ARTICLE OPEN

Check for updates

Prolonged dephasing time of ensemble of moiré-trapped interlayer excitons in WSe$_2$-MoSe$_2$ heterobilayers

Mehmet Atıf Durmuş[1], Kaan Demiralay[1], Muhammad Mansoor Khan[1], Şeyma Esra Atalay[1] and Ibrahim Sarpkaya [1]✉

The moiré superlattices of transition metal dichalcogenide heterobilayers have a pronounced effect on the optical properties of interlayer excitons (IXs) and have been intensively studied in recent years. However, the impact of moiré potentials on the temporal coherence of the IXs has not yet been investigated in detail. Here, we systematically investigate the coherence properties of both the ensemble of delocalized and the ensemble of localized IXs trapped in moiré potentials of the hexagonal boron nitride encapsulated WSe$_2$-MoSe$_2$ heterostructures. Our low-temperature first-order correlation measurements show that prolonged T_2 dephasing times with values up to 730 fs can be obtained from the ensemble of localized IXs under moderate pump powers. We observed up to almost a five-fold increase over the values we obtained from the delocalized IXs, while more than two-fold over the previously reported values of $T_2 \sim 300$ fs from the delocalized IXs. The prolonged values of T_2 dephasing times and narrow photoluminescence (PL) linewidths for the ensemble of moiré-trapped IXs compared to delocalized one indicate that dephasing mechanisms caused by exciton-low energy acoustic phonon and exciton-exciton scattering are significantly suppressed due to the presence of localization potentials. Our pump power-dependent T_2 results show that ultra-long dephasing times can be expected if the dephasing time measurements are performed with the narrow photoluminescence emission line of a single moiré-trapped IX at a low pump power regime. The prolonged values of IX dephasing times would be critical for the applications of quantum information science and the development of two-dimensional material-based nanolasers.

INTRODUCTION

Transition metal dichalcogenides (TMDCs) have been intensively studied in different research fields due to their exciting mechanical, electronic, and optical properties[1]. They have been particularly considered for the development of various optoelectronic, quantum photonic, and valleytronic devices due to their intriguing optical properties, such as direct electronic band gap in their monolayer limit[2,3], large exciton binding energies[4,5], and valley-contrasting physics[6,7]. The development of various transfer techniques has also made stacking different TMDC monolayers on top of each other possible without a lattice mismatching issue[8,9]. The van der Waals heterostructures of molybdenum (Mo) and tungsten (W) based monolayers give rise to a staggered type-II band alignment[10] and allow the formation of interlayer excitons (IXs)[11–16] (i.e., strongly Coulomb-bound electron-hole pair located in different layers) due to ultra-fast charge transfer between two monolayers[17,18]. These spatially indirect interlayer excitons possess unique optical properties compared to their intralayer counterparts, such as long spontaneous emission lifetimes[11,13], tunable photoluminescence emission[19], and permanent out-of-plane electric dipole moment[19,20]. These unique optical properties of IXs have not been utilized only for the demonstration of exciting physical phenomena such as the many-body quantum state of IXs[21] but also for the realization of various optoelectronic devices such as nanolasers with the operating wavelength in the near-infrared region[22,23] as well as transistors[24] and photodetectors[25]. Moreover, the intriguing in-plane moiré superlattices appear in heterobilayers of TMDCs due to small twist angles and/or lattice mismatching between constituent layers[26]. According to the results of theoretical studies with IXs, moiré potentials in heterobilayers of TMDC materials give rise to the localization of IX

states. Due to the periodicity of the moiré potentials along the heterobilayer, it would be feasible to create 2D arrays of quantum dots at the nanoscale[27,28]. Recent experimental studies demonstrated that IXs could be trapped and localized in quantum dot-like potentials giving rise to the appearance of narrow PL emission lines in the low-temperature PL spectra of, for example, MoSe$_2$-WSe$_2$ heterobilayer[29]. The linewidths of these localized emitters are two orders of magnitude narrower than the previously reported values of delocalized IXs[11,12,19,30] and comparable to the linewidth of single photon emitters in monolayer WSe$_2$[31] and hexagonal boron nitride (hBN)[32]. The quantum nature of the emitted light from these moiré localized emitters has also been confirmed in recent photon antibunching experiments[33]. Moreover, the effect of the strain-modulated moiré landscape on the optical properties of IXs of WSe$_2$-MoSe$_2$ heterobilayers has been investigated in detail in recent studies[34,35]. Although the pronounced effect of moiré potentials on the diffusion properties of IXs has also been shown in recent transport studies[36,37], the effect of these intrinsic localization mechanisms on the coherence properties of IXs in WSe$_2$-MoSe$_2$ heterostructures has not been studied systematically yet. Considering the well-protection of localized emitters from different dephasing mechanisms (e.g., exciton-low energy acoustic phonon interaction, and exciton-exciton scattering), one can expect to obtain long dephasing times for the trapped IXs in moiré potentials.

Here, we systematically investigate the coherence properties of both the ensemble of delocalized IXs and the ensemble of localized IXs trapped in moiré potentials of the hBN encapsulated WSe$_2$-MoSe$_2$ heterostructures. We have performed first-order correlation measurements in the time domain using a home-built free space Michelson Interferometer. Our low-temperature first-order coherence measurements show that prolonged

[1]Bilkent University UNAM – National Nanotechnology Research Center, Ankara 06800, Turkey. ✉email: sarpkaya@unam.bilkent.edu.tr
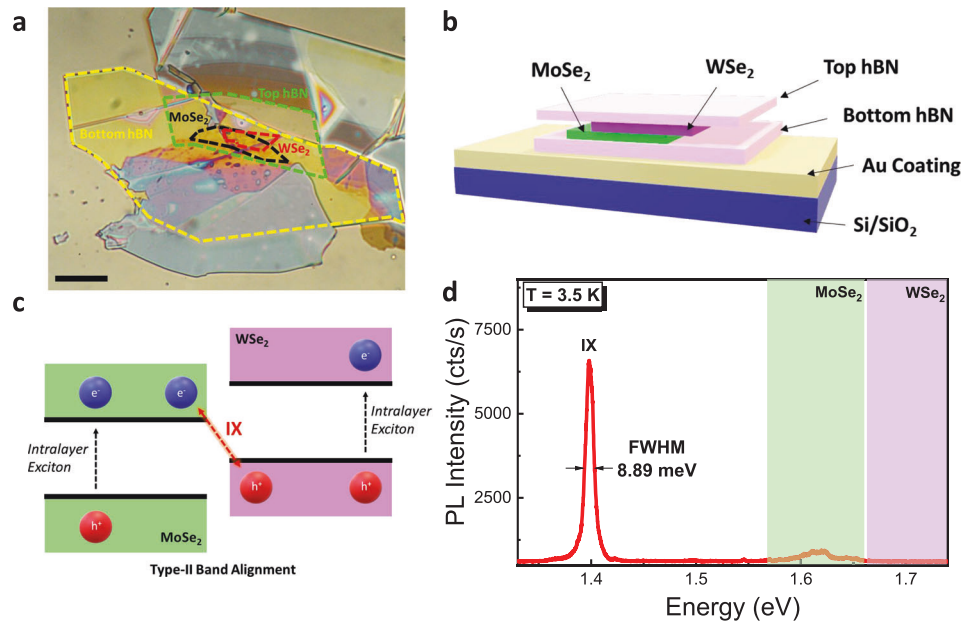
npj

Fig. 1 WSe$_2$-MoSe$_2$ heterobilayer & PL characteristics. Optical microscope image, the scale bar is 10 µm (**a**) and schematic of the hBN encapsulated WSe$_2$-MoSe$_2$ heterobilayer sample (HS1) on top of Au-coated (~100 nm) substrate (**b**). **c** Schematic of the interlayer and intralayer excitonic states in the type-II band configuration of the studied heterobilayers. IX represents the interlayer exciton. **d** Low-temperature photoluminescence (PL) spectrum of the WSe$_2$-MoSe$_2$ heterobilayer (HS1) with the IX emission appearing at ~1.4 eV under 532-nm CW laser excitation with an incident power of $P = 50$ µW. Green and purple boxes show the region of intralayer exciton PL peaks of the MoSe$_2$ and WSe$_2$, respectively.

dephasing times with values up to 730 fs can be obtained from the emission of the ensemble of localized IXs under moderate pump powers. We observed up to a five-fold increase over the values we obtained from the delocalized IXs, while more than two-fold over the previously reported values of $T_2 \sim 300$ fs from the delocalized IXs[21].

RESULTS AND DISCUSSION

Low temperature PL spectroscopy of IXs in WSe$_2$-MoSe$_2$ heterobilayers

To investigate the photophysics of IXs with the aim of measuring the dephasing times of both ensemble of delocalized spin-triplet IXs and moiré-localized IXs in the time domain, we have fabricated hBN encapsulated WSe$_2$-MoSe$_2$ heterobilayers with a nearly 0° or 60° twist angle using the well-known viscoelastic dry transfer technique[38]. Following the identification of monolayer WSe$_2$ and MoSe$_2$ flakes according to their optical microscope contrast and PL emission, hBN encapsulated heterostructures (HS) were fabricated using the viscoelastic dry stamping technique sequentially. The fabrication process details are given in the methods section and Supplementary Note 1. Figure 1a, b shows the optical microscope image and a schematic of an hBN-encapsulated WSe$_2$-MoSe$_2$ heterobilayer (HS1) on top of a 100 nm thick Au-coated substrate, respectively. As can be seen from the schematic of the electronic band diagram in Fig. 1c, the WSe$_2$-MoSe$_2$ heterostructure has a type-II band alignment. In these heterostructures, ultra-fast charge transfer happens between two monolayers within the time scale of 100 fs[17,18], and due to strong Coulomb interaction, interlayer excitons are formed in addition to intralayer excitons[11–14]. Figure 1d shows the exemplary low-temperature PL spectrum of one of the fabricated WSe$_2$-MoSe$_2$ heterobilayers (HS1). Similar to the previous studies, the PL spectrum at 3.5 K consists of a dominant spin-triplet IX PL emission in the 1.4 eV region and weak intralayer exciton emission of individual monolayers in the 1.6 and 1.7 eV regions (green and purple shaded areas in

Fig. 1d). Under relatively high pump powers (~0.4 mW), in accordance with the previous studies[39–41], we also observed the spin-singlet emission peak at ~25 meV above the spin-triplet one with very low intensity (Supplementary Note 2).

Magneto-PL spectroscopy of IXs in WSe$_2$-MoSe$_2$ heterobilayers

To further study the nature of the emitted light and determine the effective Landé g-factor of the delocalized spin-triplet IXs, we have performed magneto-PL spectroscopy at 3.5 K. We used a linearly polarized 532 nm CW laser as an excitation source and collected emitted PL under different magnetic field magnitudes. Figure 2a shows the PL spectra of spin-triplet IX under linear excitation as a function of the applied magnetic field in Faraday geometry (i.e., magnetic field perpendicular to heterobilayer). The single PL emission line of the spin-triplet IX splits into two with the increased magnetic field. The maximum splitting value of ~8 meV has been observed at 9 T. The observed splitting is due to the Zeeman shift of the energy gaps of the K and K' valleys and can be defined as $|\Delta E_{IX}| = g\mu_B B$ where g is the effective Landé g-factor, μ_B is the Bohr magneton (~58 µeV/T), and B is the strength of the applied magnetic field. As can be seen in Fig. 2c, the extracted Zeeman splitting increases linearly with the applied magnetic field. The linear fit of the experimental data in Fig. 2c provides an effective g-factor of 16.29 ± 0.07. Due to the non-vanishing valley magnetic moment contribution to the valley Zeeman splitting, the obtained value of the effective g-factor of IX of heterostructure is much larger than the corresponding g-factor of monolayer TMDC excitons (~4)[42,43]. The experimentally measured value of the g-factor for the studied heterobilayer is in very well agreement with both the predictions of theoretical study[44] and the results of the recent experimental studies[30,39–41] and confirms the nearly 60° stacking angle of the fabricated heterostructure (HS1).

Time-resolved PL spectroscopy of ensemble of delocalized and ensemble of moiré localized IXs

To probe the dynamics of both delocalized and localized IX recombination, we next performed time-resolved PL (TRPL) studies with the PL emission of fabricated heterostructures. Figure 3a, b shows the exemplary low-temperature PL spectrum of the HS1 under 532 nm pulsed laser excitation and TRPL intensity as a function of delay time, respectively. The solid red line in the plot indicates a bi-exponential fit with fast and slow lifetime components of 2.58 ± 0.05 ns and 26.05 ± 0.55 ns, respectively.

Figure 3c shows the overview of the IX PL lifetimes of different WSe_2-$MoSe_2$ heterobilayer samples. The experimentally measured PL lifetimes of delocalized IXs (HS1-HS4) are very well in agreement with the previously reported values[11–14,30]. Similar to intralayer exciton localization, one can expect longer lifetimes for trapped IXs (HS5-HS7) compared to delocalized IXs. However, the observed lifetimes of excitons (both intra- and inter-layer) are not only determined by the intrinsic homogeneous effects but also by the extrinsic inhomogeneous effects, including defects, impurities, adsorbates…, etc., introduced during the fabrication process of TMDC monolayers and their heterobilayers. Those inhomogeneous
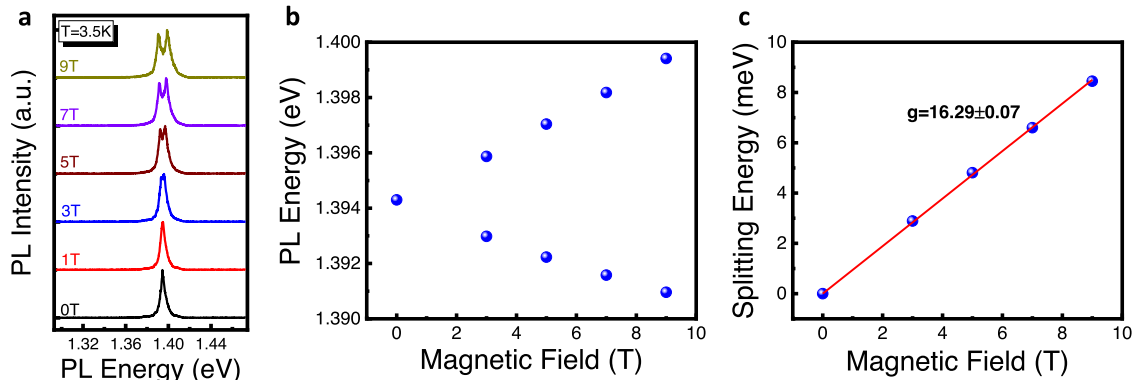

Fig. 2 Zeeman splitting of IX emission in the WSe_2-$MoSe_2$ heterobilayer sample. a The PL spectra for spin-triplet IX as a function of the strength of an applied out-of-plane magnetic field under 532 nm CW laser excitation. **b** The PL peak energies as a function of the applied magnetic field. **c** The Zeeman splitting measured for spin-triplet IX with an effective g-factor of 16.29 ± 0.07. Data are recorded at 3.5 K.
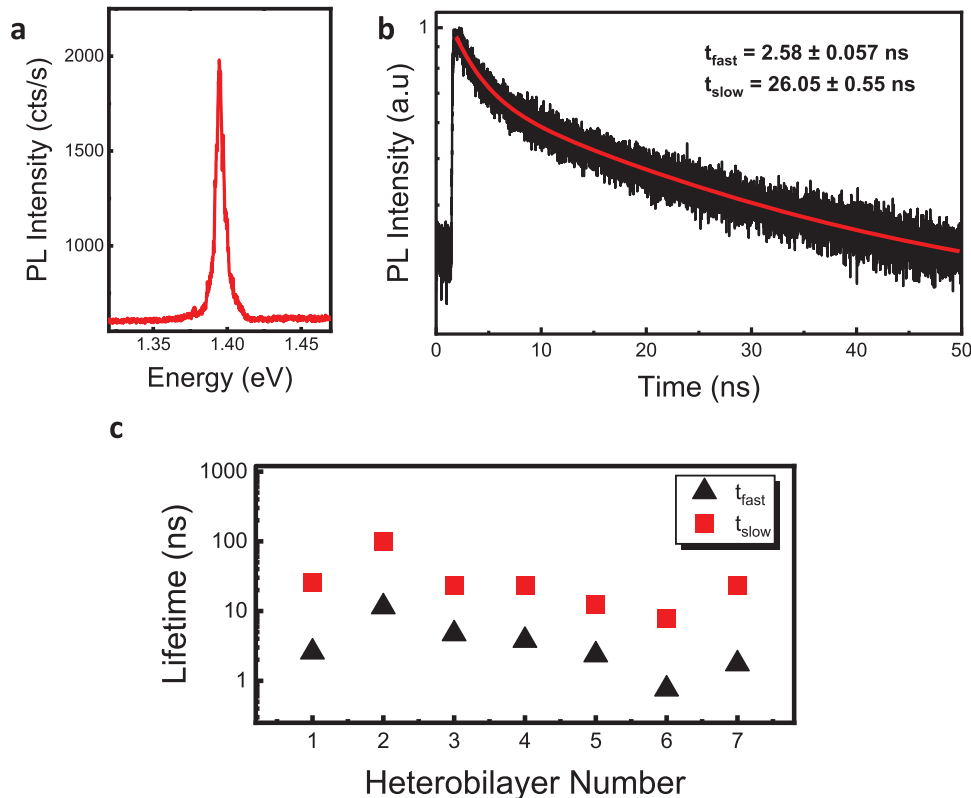

Fig. 3 Time-resolved PL of the WSe_2-$MoSe_2$ heterobilayer samples. a PL spectrum of the spin-triplet IX from HS1 under 20-MHz pulsed laser excitation at 532 nm with an incident power of $P = 6$ μW. The spectrum was filtered by using an 850 nm hard-coated long-pass filter. **b** Time-resolved PL intensity of the same IX emission as a function of delay time after pulsed excitation at 532 nm. The red line in the plot indicates a bi-exponential fit featuring fast and slow lifetime components of 2.58 ± 0.05 ns and 26.05 ± 0.55 ns, respectively. **c** Overview of the IX lifetimes of the fabricated WSe_2-$MoSe_2$ heterobilayer samples. Red squares indicate the slow decay components, while the black triangles indicate the fast decay components of the IX PL emission lifetime. Data are recorded at 3.5 K.
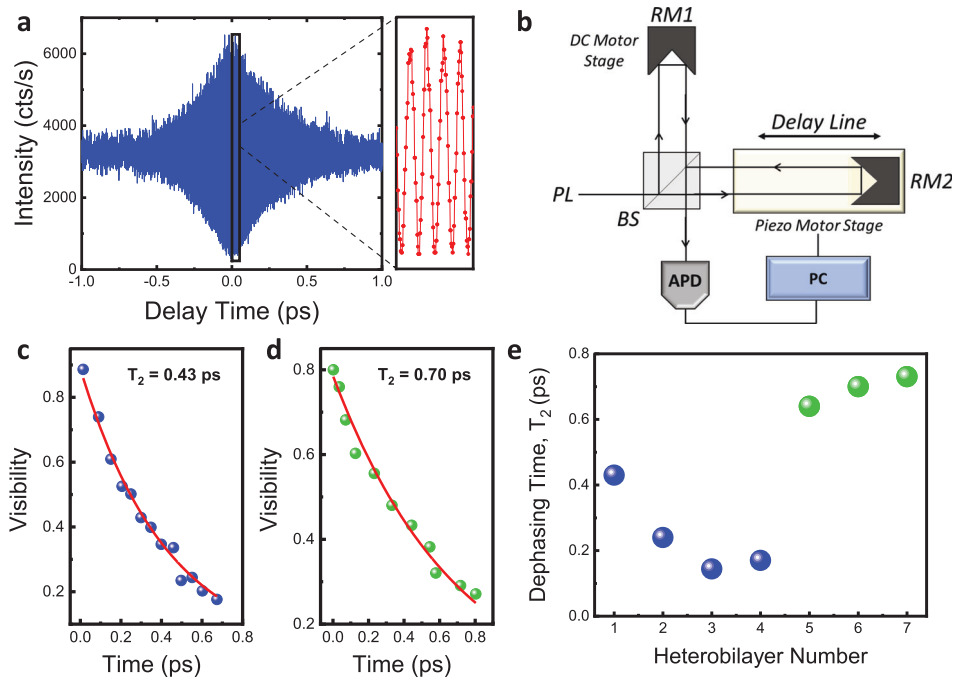
Fig. 4 IX dephasing time measurements of WSe$_2$-MoSe$_2$ heterobilayers using a home-built Michelson Interferometer. a Interferogram of the first order coherence function $g^{(1)}(\tau)$ of the IX of HS1. The zoomed-in version of the black box in the right panel shows pronounced fringe contrast near zero delay time. **b** Schematic of the home-built Michelson interferometer with two movable mirror arms. The measurement is done with the piezo-motor arm with a step size of 20 nm. BS, beam splitter; RM, retro mirror; APD, avalanche photodiode; PC, computer control. **c** The fringe visibility as a function of delay time for the delocalized IX emission of the WSe$_2$-MoSe$_2$ heterobilayer (HS1). It shows a mono-exponential decay, and the red line indicates the fit that gives a value of $T_2 = 0.43$ ps. **d** The fringe visibility as a function of delay time for the ensemble of moiré localized IX emission of the WSe$_2$–MoSe$_2$ heterobilayer (HS6) **e** Comparison between the decoherence time values of the ensemble of delocalized and moiré localized IXs of the fabricated WSe$_2$-MoSe$_2$ heterostructures. The longest coherence time is found to be $T_2 = 0.73$ ps. Data are recorded at 3.5 K.

effects can give rise to the occurrence of very efficient, long-lived non-radiative recombination decay channels. The effect of localization (extrinsically strain-induced) on the lifetime of IXs has been studied in detail in one of the two recent studies[45,46]. Similar to the idea developed in that study[45], highly mobile delocalized interlayer excitons with longer diffusion lengths in our heterobilayers (HS1–HS4) can easily explore those long-lived non-radiative recombination centers, and their lifetimes can be dominated by radiative recombination from those long-lived energy levels to the ground state. However, due to the localization either in an extrinsically strain-induced potential well (in ref. [45]) or intrinsic moiré potential in our case, trapped IXs with limited diffusion lengths rarely encounter those centers. So, the contribution of the non-radiative decay process to the observed lifetime of localized IXs is rather small and gives rise to observed shorter or similar lifetimes of localized IXs compared to the delocalized one in Fig. 3. We also note that due to shorter lifetimes and diffusion lengths of intralayer excitons compared to IXs, the aforementioned effect of localization on the suppression of non-radiative decay channels will be rather small. Accordingly, one can see the direct contribution of homogeneous effects in the lifetime of intralayer excitons in contrast to interlayer excitons.

Dephasing time measurements of delocalized and moiré localized IXs

Although the pronounced effect of moiré potentials on the diffusion properties of IXs has been shown in recent transport studies[36,37], the effect of those intrinsic localization mechanisms on the coherence properties of IXs in WSe$_2$-MoSe$_2$ heterostructures has remained elusive until now. We next study the coherence properties of both ensemble of delocalized and the ensemble of moiré-trapped IXs. We present dephasing time (T_2)

measurements of these IXs in the time domain by measuring the first-order correlation function $g^{(1)}(\tau)$ with a home-built Michelson interferometer. The free-space home-built Michelson interferometer in Fig. 4b consists of a 50:50 beam splitter and two retroreflectors one is fixed on the DC motor stage the other is on the piezo motor stage to create a delay time. Figure 4a shows an example of an interferogram of light from the spin-triplet IX of HS1. The right panel of Fig. 4a shows pronounced fringe contrast (~92%) near zero delay time obtained by a delay line with a retroreflector and a stepping resolution of 20 nm. Using the relation $V(\tau) = \frac{I_{max} - I_{min}}{I_{max} + I_{min}}$, where I_{max} and I_{min} are the fringe maxima and minima identified from distinct fringe patterns at varying delay times, the visibility of the fringes was estimated. Figure 4c shows $V(\tau)$ as a function of delay time, which can be fit mono-exponentially with the function of $g^{(1)}(\tau) \sim e^{-\frac{|\tau|}{T_2}}$. The dephasing time of the spin-triplet IX was determined as $T_2 = 0.43$ ps for HS1. As seen from the overview graph in Fig. 4e, we have obtained T_2 values between 160 and 430 fs (blue circles in Fig. 4e) for the ensemble of delocalized IXs (HS1-HS4), which are very well in agreement with the previously measured values[21]. Our pump power-dependent PL measurements at low temperatures in Supplementary Fig. 2 indicate that 0D hexagonal moiré superlattices may have been distorted in these heterostructures. Otherwise, as observed in previous studies[29,47], as a signature of moiré-trapped IXs, we could have seen sharp and narrow emission lines with linewidth values of about 100 μeV at low pump powers. We have ruled out the complete absence of hexagonal moiré superlattice as a possible cause of the disappearance of sharp and narrow emission lines. The absence of moiré superlattice has been observed in the case of commensurate and rotationally aligned CVD-grown heterobilayers due to small lattice distortion[36]. However, because of the lattice mismatch and twist angle
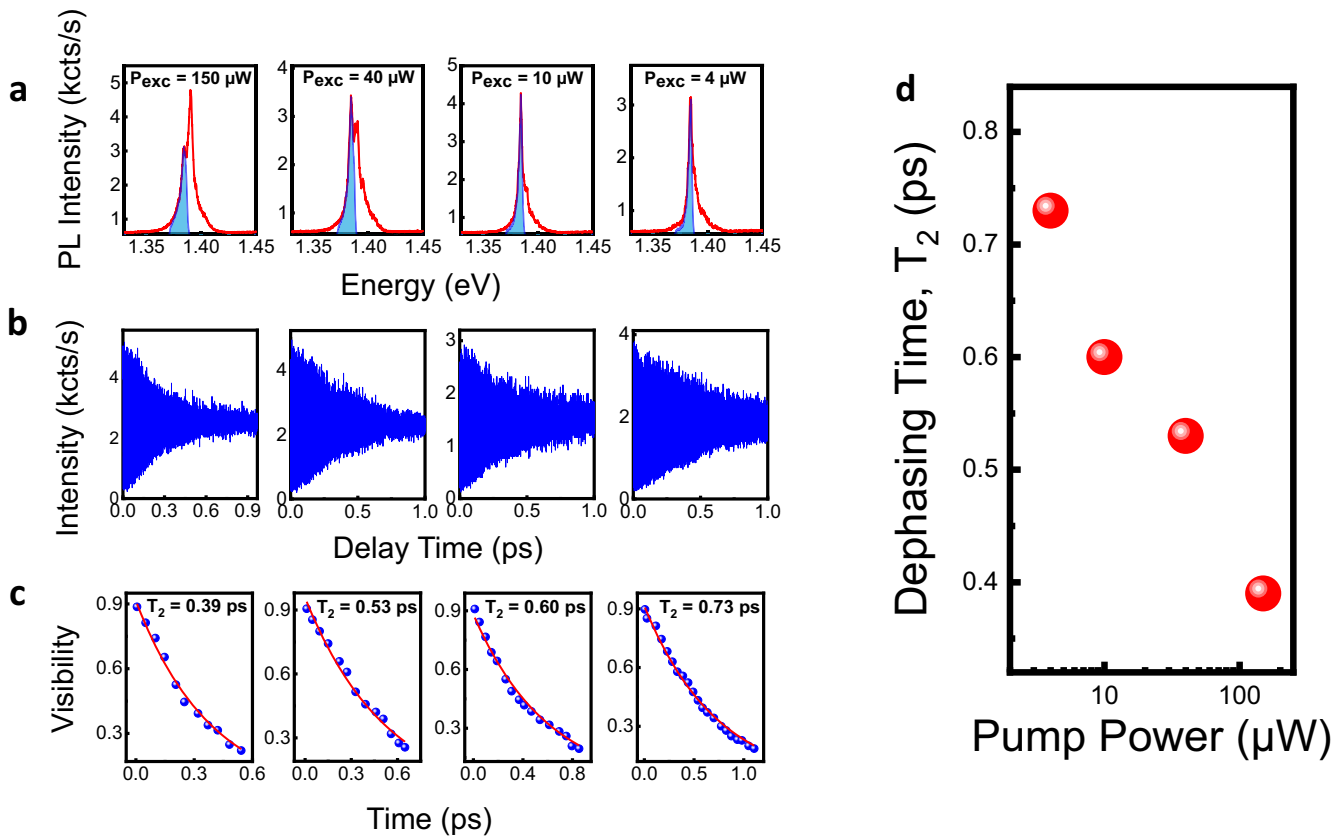
Fig. 5 Pump power-dependent dephasing time (T₂) of moiré-trapped IXs. a Low- temperature PL spectra of ensemble of 0D moiré localized IXs under different pump powers. **b** Corresponding interferograms of the first order coherence functions $g^{(1)}$ (τ) obtained by sending the filtered PL (blue region) in (**a**) into a Michelson Interferometer. **c** The corresponding fringe visibilities as a function of delay time for the localized IX emission of the WSe₂ -MoSe₂. They show a mono-exponential decay, and the red lines in each plot indicate the fit that gives the values of T₂. **d** Overview of the T_2 dephasing times of the fabricated WSe₂-MoSe₂ heterobilayer sample (HS7) under different pump powers. Data are recorded at 3.5 K.

between the individual layers in our mechanically stacked heterobilayers, the formation of moiré superlattice is always expected. Moreover, the recent studies[34,35] showed that mainly strain-induced distortion of moiré superlattice landscape can cause the formation of 2D, 1D, and 0D domains in the different parts of a sample. We attribute the disappearance of sharp and narrow PL emission peaks at low pump power regimes in these samples (HS1–HS4) to the distortion of 0D confinement potential due to the unintentional strain that might have been created during the fabrication process of heterostructures. As shown in one of the above studies using piezoresponse force microscopy (PFM), the strain created during the fabrication process of the heterobilayers can change the shape and period of the moiré pattern and transform the 0D hexagonal moiré superlattice into 1D moiré superlattice. According to the 2D harmonic trap model developed in the same study, the 1D moiré trap can possess a high density of states with closely spaced excitonic levels, whereas the 0D moiré potential can host only a few bound states. Because of the higher density states of the 1D moiré trap, radiative recombination can happen from multiple levels giving rise to the broadening of the PL spectrum even at a low pump power regime. However, for the 0D quantum-dot-like confinement potentials, the lowest exciton state most likely dominates the PL spectrum, and one can see those narrow and sharp PL peaks at low pump power and temperatures. The PL lineshapes (broad (HS1–HS4) and sharp and narrow (HS5, HS6, HS7) observed from our heterobilayers at low pump power regimes indicate that 0D confinement might have been distorted in some samples due to unintentional strain created during the fabrication process.

However, in some of the other fabricated heterostructures (HS5-HS7), 0D hexagonal moiré superlattices have been successfully formed. As can be seen from the pump power dependence of the IX emission in these heterostructures, we observed sharp and narrow emission lines with the FWHM of a few hundred µeV in the low pump power regime (Supplementary Figs. 3–5). Once the pump power is increased, the narrow and sharp emission lines evolve to broad ensemble IX peaks. We further performed magneto-PL measurements for these moiré-localized IXs under low pump power and obtained an effective g-factor of 15.9 ± 03 (Supplementary Fig. 6). As confirmed in a recent study[40], both broad ensemble band and narrow emission lines originate from the localization of the IXs in 0D quantum-dot-like moiré potentials. Because interferometric measurements require as many photons as possible, we have performed dephasing time measurements under moderate pump powers where sharp and narrow emission lines evolve to a broad ensemble band of moiré localized IX emission. Figures 4d, 5c and Supplementary Fig. 7 show the fringe visibility as a function of delay time for the broad ensemble of moiré localized IXs. The measured values of decoherence time $T_2 = 0.64$ ps for HS5, 0.7 ps for HS6 and 0.73 for HS7 (green circles in Fig. 4e) are two- to almost fivefold longer compared to the values we obtained from the ensemble of delocalized IXs (blue circles in Fig. 4e), while it is more than two-fold prolonged compared to previously measured limited values of ~300 fs[21].

Dephasing mechanism of IXs in WSe₂-MoSe₂ heterobilayers
To further probe the dephasing mechanism of IXs in WSe₂-MoSe₂ heterobilayers, we have also performed pump power-dependent
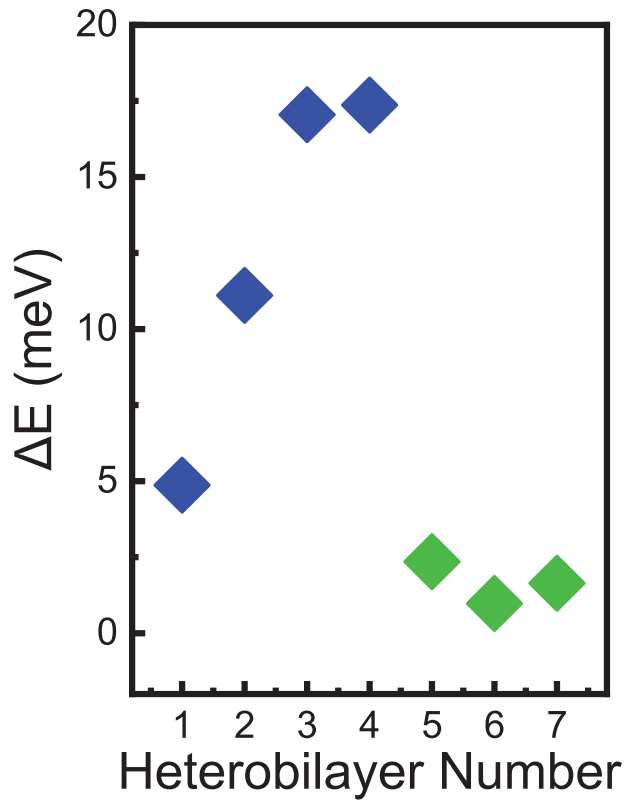
Fig. 6 Spectral linewidth study of IXs. Energy difference (ΔE) between the spectral linewidth obtained from PL spectra and calculated from the measured T_1 and T_2 data in Figs. 3c and 4e for delocalized (blue diamonds) and moiré-trapped (green diamonds) IXs.

T_2 measurements in Fig. 5 for the moiré trapped IXs. Starting from the high pump power regime, we tried to obtain T_2 data under the lowest pump power we could achieve. It was impossible to perform conclusive T_2 measurements below 1 µW pump power due to the less PL signal of the single or few moiré trapped IXs as can be seen from the pump power dependent PL in Supplementary Fig. 5. Nevertheless, the increase of the T_2 with the decreasing pump power in Fig. 5 indicates that ultra-long dephasing times could be expected if the dephasing time measurements are performed with the narrow PL emission line of a single moiré localized IX at a low pump power regime. In future studies, this can be achieved by integrating the heterobilayer into optical cavities[48]. Our results also indicate that pump power induced exciton-exciton scattering is the main dephasing mechanism for the investigated IXs in TMDC heterobilayers.

The prolonged values of decoherence time for the ensemble of moiré-trapped IXs compared to delocalized IXs (i.e., absence of 0D moiré potential) can be attributed to the suppression of dephasing caused by IX-low energy acoustic phonon[21] and exciton-exciton scattering[49]. A similar effect of spatial localization on the coherence properties of excitons has also been observed for the positively charged trion (X^+) of monolayer $MoSe_2$[50].

To further emphasize the effect of localization on the dephasing time of the IXs, in Fig. 6, we plot the energy difference (ΔE) between the spectral linewidth values obtained from the time-integrated PL emission and calculated from the measured T_1 and T_2 times (Fig. 3c and Fig. 4e) with the well-known formula $\Gamma = \frac{\hbar}{T_1} + \frac{2\hbar}{T_2}$[51]. For the calculated linewidths, we consider the possible broadening coming from the fast component of T_1, which is rather small (Supplementary Fig. 8), such that the calculated linewidth is dominated by T_2 alone ($\Gamma \sim \frac{2\hbar}{T_2}$). As can be

seen from Fig. 6, ΔE values of the delocalized excitons up to 17 meV (blue diamonds) are much larger than the corresponding values of moiré-tapped IXs with the smallest value of 0.9 meV (green diamonds). The small values of ΔE in the case of IX localization indicate that the contribution of inhomogeneous linewidth broadening caused by charge fluctuations in the vicinity of an emitter and by strong repulsive exciton-exciton scattering (i.e., excitation-induced dephasing)[49] is significantly suppressed.

In conclusion, we have performed low-temperature dephasing time measurements in the time domain for the ensemble of delocalized and moiré-localized IXs of hBN-encapsulated WSe_2-$MoSe_2$ heterobilayers. The measured values of IX dephasing time T_2 are two to almost five-fold longer compared to the values we obtained from the ensemble of delocalized IXs, while it is more than twofold prolonged compared to previously reported values of ~300 fs[21]. We attribute the enhancement of IX dephasing time to the suppression of the dephasing mechanisms caused by the interaction of an IX with the other IXs and low-energy acoustic phonons. We also note that ultra-long dephasing times can be expected if the dephasing time measurements are performed with the narrow PL emission lines of a single moiré localized IX at a low pump power regime. The prolonged values of IX dephasing times would be critical for the applications of quantum information science as well as the development of two-dimensional material-based nanolasers[52].

METHODS

Sample preparation

Each layer of monolayer $MoSe_2$ and WSe_2 and the encapsulation layers of hBN (obtained from 2D Semiconductors) were mechanically exfoliated onto polydimethylsiloxane. Before stacking these 2D layers, their thicknesses are evaluated with their color contrast in the optical microscope, then confirmed by PL-spectroscopy. The lattice directions of the exfoliated $MoSe_2$ and WSe_2 monolayers were identified with the optical microscope using the edge identification method[53]. After identifying the zigzag edges, these prepared 2D layers were successfully stacked and aligned ($\theta \sim 0°$ or 60°) onto a ~100 nm Au-coated Si/SiO_2 substrate using the dry transfer technique. Room temperature PL spectroscopy (under 532 nm CW laser excitation with 100 µW power) was performed to check the nature of the fabricated heterobilayers. It was confirmed that both intralayer and interlayer excitons could be observed in the integrated (1 s integration for the intralayer region, 60 s integration for the interlayer region) PL measurements.

Low-temperature optical spectroscopy

After the room temperature PL measurements, the low temperature (3.5 K) PL measurements were performed using the home-built µ-PL setup. The heterobilayer samples were mounted on a piezoelectric stage for nano-step positioning in the closed-cycle cryostat (Attodry 1000) setup. For the excitation source, a picosecond pulsed laser diode operating at 532 nm under both CW and the pulsed mode was used, and the emission was collected through a low-temperature compatible microscope objective (0.82 NA) and filtered by a 550 nm long-pass filter (Thorlabs FEL0550) for observing the whole spectrum. To record the PL spectra, a 750 mm focal length spectrograph (Princeton Instrument SpectraPro HRS-750) along with a liquid nitrogen-cooled silicon charge-coupled device camera (PyLoN) was used together. To observe the Zeeman splitting, which is used to define the g factors of the interlayer excitons, the built-in super-conducting magnet inside the cryostat was used to apply out-of-plane direction magnetic fields from 0 T up to 9 T. Before sending the emission through the home-built Michelson interferometer via single-mode fiber, the emitted light was further filtered by an 850 nm long-pass filter (Thorlabs FELH0850) or

880 nm (Thorlabs FBH880) and 905 nm hard coated (FBH905–10) band-pass filters according to the interlayer exciton PL characteristics such as its location and its linewidth.

Dephasing time measurements with a Michelson Interferometer

A home-built Michelson interferometer with two moveable retro mirrors was constructed to measure the interlayer excitons' dephasing time T_2 in our heterobilayers. Each retro mirror arm featured a different motorized stage managed by a LabVIEW program. One retro mirror was on the DC motorized stage (Thorlabs DDS050) with a 5 µm step size and the other retro mirror was on the piezo motor stage (Thorlabs PIA13) with a 20 nm step size. These motors were operated by the appropriate controllers (Thorlabs KBD101 and TIM101), which in turn were controlled by the LabVIEW program. The adjustment of the time-zero (where the two mirrors have the same distance from the beam-splitter) was done with the DC motorized stage due of its relatively high speed and step size. Following this adjustment, the first-order correlation function $g^{(1)}(\tau)$ measurement is done with only the piezo motor stage due to its small step size that can resolve the fringes. Together with the piezo stage, the data acquisition device PicoQuant HydraHarp 400 was used with a silicon single photon avalanche diode with a photon timing resolution of 50 ps (Micro Photon Devices-PDM series) to obtain the interferogram of the interlayer excitons. By using various maxima and minima points of the obtained fringes, the visibility as a function of delay time plot was obtained and monoexponentially fitted to calculate the dephasing time (T_2) of the interlayer excitons.

DATA AVAILABILITY

The datasets used and/or analyzed during the current study available from the corresponding author on reasonable request.

REFERENCES

1. Yang, E.-H., Datta, D., Ding, J. & Hader, G. *Synthesis, Modelling and Characterization of 2D Materials and their Heterostructures*, 1st edn, (Elsevier, 2020).
2. Mak, K. F., Lee, C., Hone, J., Shan, J. & Heinz, T. F. Atomically thin MoS2: a new direct-gap semiconductor. *Phys. Rev. Lett.* **105**, 136805 (2010).
3. Splendiani, A. et al. Emerging photoluminescence in monolayer MoS2. *Nano Lett.* **10**, 1271–1275 (2010).
4. He, K. et al. Tightly bound excitons in monolayer WSe2. *Phys. Rev. Lett.* **113**, 026803 (2014).
5. Chernikov, A. et al. Exciton binding energy and nonhydrogenic rydberg series in monolayer WS2. *Phys. Rev. Lett.* **113**, 076802 (2014).
6. Xiao, D., Liu, G.-B., Feng, W., Xu, X. & Yao, W. Coupled spin and valley physics in monolayers of MoS_2 and other group-VI dichalcogenides. *Phys. Rev. Lett.* **108**, 196802 (2012).
7. Cao, T. et al. Valley-selective circular dichroism of monolayer molybdenum disulphide. *Nat. Commun.* **3**, 887 (2012).
8. Geim, A. K. & Grigorieva, I. V. Van der Waals heterostructures. *Nature* **499**, 419–425 (2013).
9. Ajayan, P., Kim, P. & Banerjee, K. Two-dimensional van der Waals materials. *Phys. Today* **69**, 38–44 (2016).
10. Kang, J., Tongay, S., Zhou, J., Li, J. & Wu, J. Band offsets and heterostructures of two-dimensional semiconductors. *Appl. Phys. Lett.* **102**, 012111 (2013).
11. Rivera, P. et al. Observation of long-lived interlayer excitons in monolayer $MoSe_2$–WSe_2 heterostructures. *Nat. Commun.* **6**, 6242 (2015).
12. Nagler, P. et al. Interlayer exciton dynamics in a dichalcogenide monolayer heterostructure. *2D Mater.* **4**, 025112 (2017).
13. Miller, B. et al. Long-lived direct and Indirect Interlayer Excitons in van der Waals Heterostructures. *Nano Lett.* **17**, 5229–5237 (2017).
14. Rivera, P. et al. Interlayer valley excitons in heterobilayers of transition metal dichalcogenides. *Nat. Nanotechnol.* **13**, 1004–1015 (2018).
15. Jiang, Y., Chen, S., Zheng, W., Zheng, B. & Pan, A. Interlayer exciton formation, relaxation, and transport in TMD van der Waals heterostructures. *Light Sci. Appl.* **10**, 72 (2021).
16. Sarpkaya, I. Optical properties of semiconducting transition metal dichalcogenide materials, In *Synthesis, Modeling, and Characterization of 2D Materials, and Their Heterostructures* (eds. Yang, E-H., Datta, D., Ding, J. & Hader, G.) 57–75 (Elsevier, 2020).
17. Hong, X. et al. Ultrafast charge transfer in atomically thin MoS2/WS2 heterostructures. *Nat. Nanotechnol.* **9**, 682–686 (2014).
18. Ceballos, F., Bellus, M. Z., Chiu, H.-Y. & Zhao, H. Ultrafast charge separation and indirect exciton formation in a MoS2–MoSe2 van der Waals heterostructure. *ACS Nano* **8**, 12717–12724 (2014).
19. Ciarrocchi, A. et al. Polarization switching and electrical control of interlayer excitons in two-dimensional van der Waals heterostructures. *Nat. Photonics* **13**, 131–136 (2019).
20. Jauregui, L. A. et al. Electrical control of interlayer exciton dynamics in atomically thin heterostructures. *Science* **366**, 870–875 (2019).
21. Sigl, L. et al. Signatures of a degenerate many-body state of interlayer excitons in a van der Waals heterostack. *Phys. Rev. Res.* **2**, 042044 (2020).
22. Liu, Y. et al. Room temperature nanocavity laser with interlayer excitons in 2D heterostructures. *Sci. Adv.* **5**, eaav4506 (2019).
23. Paik, E. Y. et al. Interlayer exciton laser of extended spatial coherence in atomically thin heterostructures. *Nature* **576**, 80–84 (2019).
24. Unuchek, D. et al. Room-temperature electrical control of exciton flux in a van der Waals heterostructure. *Nature* **560**, 340–344 (2018).
25. Lukman, S. et al. High oscillator strength interlayer excitons in two-dimensional heterostructures for mid-infrared photodetection. *Nat. Nanotechnol.* **15**, 675–682 (2020).
26. Zhang, C. et al. Interlayer couplings, moiré patterns, and 2D electronic superlattices in MoS2/WSe2 hetero-bilayers. *Sci. Adv.* **3**, e1601459 (2017).
27. Yu, H., Liu, G.-B., Tang, J., Xu, X. & Yao, W. Moiré excitons: from programmable quantum emitter arrays to spin-orbit–coupled artificial lattices. *Sci. Adv.* **3**, e1701696 (2017).
28. Wu, F., Lovorn, T. & MacDonald, A. H. Theory of optical absorption by interlayer excitons in transition metal dichalcogenide heterobilayers. *Phys. Rev. B* **97**, 035306 (2018).
29. Seyler, K. L. et al. Signatures of moiré-trapped valley excitons in MoSe2/WSe2 heterobilayers. *Nature* **567**, 66–70 (2019).
30. Nagler, P. et al. Giant magnetic splitting inducing near-unity valley polarization in van der Waals heterostructures. *Nat. Commun.* **8**, 1551 (2017).
31. Srivastava, A. et al. Optically active quantum dots in monolayer WSe2. *Nat. Nanotechnol.* **10**, 491–496 (2015).
32. Korkut, H. & Sarpkaya, İ. Controlling the photoluminescence of quantum emitters in hexagonal boron nitride by external magnetic fields. *2D Mater.* **10**, 015004 (2022).
33. Baek, H. et al. Highly energy-tunable quantum light from moiré-trapped excitons. *Sci. Adv.* **6**, eaba8526 (2020).
34. Zhao, S. et al. Excitons in mesoscopically reconstructed moiré heterostructures. *Nat. Nanotechnol.* **18**, 572–579 (2023).
35. Bai, Y. et al. Excitons in strain-induced one-dimensional moiré potentials at transition metal dichalcogenide heterojunctions. *Nat. Mater.* **19**, 1068–1073 (2020).
36. Choi, J. et al. Moiré potential impedes interlayer exciton diffusion in van der Waals heterostructures. *Sci. Adv.* **6**, eaba8866 (2020).
37. Yuan, L. et al. Twist-angle-dependent interlayer exciton diffusion in WS2–WSe2 heterobilayers. *Nat. Mater.* **19**, 617–623 (2020).
38. Castellanos-Gomez, A. et al. Deterministic transfer of two-dimensional materials by all-dry viscoelastic stamping. *2D Mater.* **1**, 011002 (2014).
39. Liu, E. et al. Signatures of moiré trions in WSe_2/$MoSe_2$ heterobilayers. *Nature* **594**, 46–50 (2021).
40. Brotons-Gisbert, M. et al. Moire-trapped interlayer trions in a charge-tunable WSe_2/$MoSe_2$ heterobilayer. *Phys. Rev. X* **11**, 031033 (2021).
41. Wang, T. et al. Giant Valley-Zeeman splitting from spin-singlet and spin-triplet interlayer excitons in WSe2/MoSe2 heterostructure. *Nano Lett.* **20**, 694–700 (2020).
42. Srivastava, A. et al. Valley Zeeman effect in elementary optical excitations of monolayer WSe2. *Nat. Phys.* **11**, 141–147 (2015).
43. MacNeill, D. et al. Breaking of valley degeneracy by magnetic field in monolayer MoSe2. *Phys. Rev. Lett.* **114**, 037401 (2015).
44. Woźniak, T., Faria Junior, P. E., Seifert, G., Chaves, A. & Kunstmann, J. Exciton g factors of van der Waals heterostructures from first-principles calculations. *Phys. Rev. B* **101**, 235408 (2020).
45. Wang, W. & Ma, X. Strain-Induced trapping of indirect excitons in MoSe2/WSe2 heterostructures. *ACS Photonics* **7**, 2460–2467 (2020).
46. Kremser, M. et al. Discrete interactions between a few interlayer excitons trapped at a MoSe2–WSe2 heterointerface. *Npj 2D Mater. Appl* **4**, 1–6 (2020).

47. Tran, K. et al. Evidence for moiré excitons in van der Waals heterostructures. *Nature* **567**, 71–75 (2019).

48. Förg, M. et al. Cavity-control of interlayer excitons in van der Waals heterostructures. *Nat. Commun.* **10**, 3697 (2019).

49. Erkensten, D., Brem, S. & Malic, E. Exciton-exciton interaction in transition metal dichalcogenide monolayers and van der Waals heterostructures. *Phys. Rev. B* **103**, 045426 (2021).

50. Shepard, G. D. et al. Trion-species-resolved quantum beats in MoSe2. *ACS Nano* **11**, 11550–11558 (2017).

51. Sarpkaya, I. et al. Prolonged spontaneous emission and dephasing of localized excitons in air-bridged carbon nanotubes. *Nat. Commun.* **4**, 2152 (2013).

52. Qian, C. et al. Lasing of Moiré trapped MoSe2/WSe2 interlayer excitons coupled to a nanocavity. Preprint at https://arxiv.org/abs/2302.07046 (2023).

53. Guo, Y. et al. Distinctive in-plane cleavage behaviors of two-dimensional layered materials. *ACS Nano* **10**, 8980–8988 (2016).

AUTHOR CONTRIBUTIONS

I.S. and M.A.D. conceived and designed the experiments. M.A.D. and M.M.K. fabricated WSe$_2$-MoSe$_2$ heterostructures. M.A.D. and Ş.E.A. fabricated additional heterobilayers during the revision process of the manuscript. M.A.D. and I.S. carried out the optical experiments and analyzed the data. K.D. performed all the necessary work for LabVIEW program control of the Michelson Interferometer. M.A.D. and I.S. co-wrote the manuscript. All authors contributed to scientific discussions.

COMPETING INTERESTS

The authors declare no competing interests.

ADDITIONAL INFORMATION

Supplementary information The online version contains supplementary material available at https://doi.org/10.1038/s41699-023-00429-6.

Correspondence and requests for materials should be addressed to Ibrahim Sarpkaya.

Reprints and permission information is available at http://www.nature.com/reprints

Publisher's note Springer Nature remains neutral with regard to jurisdictional claims in published maps and institutional affiliations.